# Open-Circuit Photopotential Characterization of Photoelectrochemical Activities of Au - Modified $TiO_2$ Nanorods

Xiao Li and Shanlin Pan

Department of Chemistry and Biochemistry, The University of Alabama, Tuscaloosa, AL 35487, United States

*Corresponding Author E-mail Address: span1@ua.edu

ABSTRACT

The Open Circuit Potential (OCP) of a semiconductor electrode can be used to quantify the transient photopotential ($E_p$), which represents wavelength-dependent charge accumulation and relaxation kinetics of a photoelectrode. Here OCP responses of a plasmonic Au@$TiO_2$ nanorods (NRs) photoelectrode can be quantified without causing electrochemical corrosion of Au. The photogenerated charge accumulation kinetics data based on the wavelength-dependent growth rates of $|E_p|$ can resolve the plasmonic effects on photoelectrochemistry (PEC) of Au@$TiO_2$ NRs. Data fitting with Kohlrausch-Williams-Watts (KWW) stretched exponential kinetics model illustrates the complex charge relaxations at the Au/$TiO_2$ Schottky contact, from which long relaxation lifetimes with broad lifetime distributions can be obtained. This is attributed to the abundant deep defects in the nanostructure $TiO_2$, which has been strongly confirmed by reducing the oxygen vacancies using a post-thermal annealing treatment. Single-particle dark-field scattering (DFS) spectrum is measured with a tunable wavelength light source to support visible light activities of PEC characteristics of Au@$TiO_2$ NRs. Light scattering spectra of > 200 single Au@$TiO_2$ NRs particles are collected to compare directly with PEC responses of OCP of the ensemble Au@$TiO_2$ NRs.

Keywords: Photoelectrochemistry, Surface plasmon, nanoparticle, single particle imaging, dark field scattering

## 1. Introduction

Surface plasmon resonance (SPR) refers to the collective oscillation motions of surface electrons of nanostructured noble metals such as Au, Ag, and Cu under resonance optical excitations. These metals have a unique negative refractive index that would support SPR activities under light

illumination. SPR plays a critical role in molecular spectroscopy enhancement[1] and ultrasensitive chemical sensing.[2-4] Due to the strong light absorption and field localization of SPR metals, they can be utilized for chemical fuel generation via photoelectrochemical (PEC) reactions[5-10] at the surface of a semiconductor under sunlight illumination. As reviewed in our recent publication,[11] SPR metals can be used to modify a metal oxide photoelectrode for PEC reactions including solar water splitting, $CO_2$ reduction, and selective oxidation of amines.[12-14] As shown in **Figure 1**, SPR-enabled PEC reaction is highly sensitive to 1) surface attachment chemistry and distance of plasmonic metal on semiconductor surface (**Figure 1A**), 2) bandgap and energy levels of the semiconductor electrode, respective to redox potentials of a half-reaction (**Figure 1B & C**), 3) catalytic capability of the SPR metal and semiconductor surface to lower overpotential of a half-reaction, and 4) potential surface chemistry transformation such as corrosion of plasmonic metal and semiconductor materials under PEC reaction conditions.

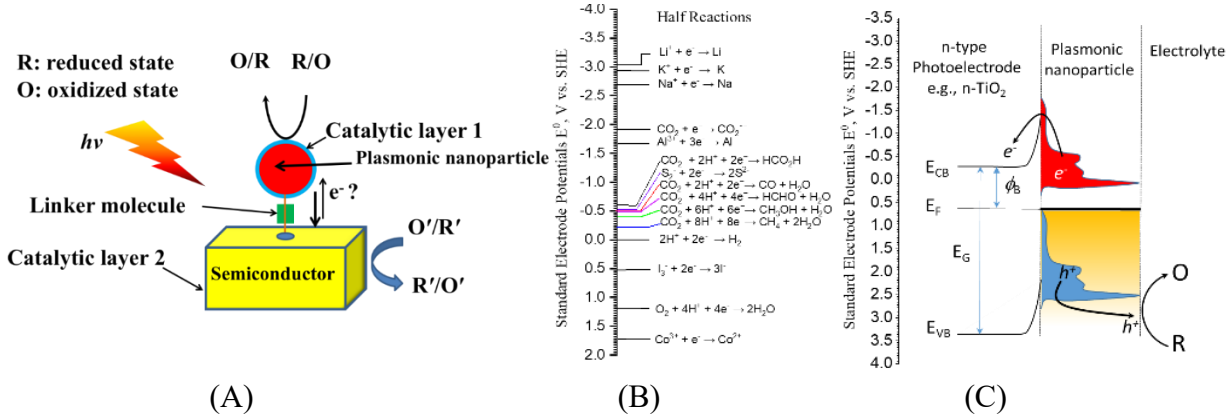


(A) (B) (C)

**Fig. 1**. ( A ) Schematic of catalytic and surface plasmon-mediated semiconductor system for enhanced solar energy harvesting and conversion by optimizing the spectrum overlapping and interfaces, (B) example half-reactions and their redox potentials relevant to water splitting and $CO_2$ reduction and other energy storage systems, and (C) schematic of energy diagram and charge separation of plasmonic nanoparticle-modified n-type photoanode for photocatalytic conversion of R to O. *Figure reproduced with permission from reference* [11] *Copyright 2023, Elsevier.*

We recently reported plasmonic metal enhanced PEC water splitting at visible light sensitive hematite photoanode in either embedded configuration[15] or top configuration.[16] PEC activities of only UV light-sensitive photoelectrodes such as $TiO_2$ would exhibit interesting PEC switch behavior when UV excitation is switched to visible light.[17] Such PEC enhancement activities can also be obtained with $TiO_2$ nanowires when coated with Au[18] and Ag NPs according to our studies.[19] Regarding SPR-enhanced PEC activities of n-type photoanode in aqueous solution, water splitting reaction $H_2O$ $-4e^- \rightarrow 4H^+ + O_2$ takes place primarily through four major mechanisms,[20] including 1) direct electron transfer from plasmonic metallic NPs to the semiconductor (**Figure 1C**),[21-29] 2) enhanced light absorption cross-section of the semiconductor upon plasmonic metal modification,[15] 3) efficient scattering mediated by SPR (far-field effect), which leads to an extended optical pathway for photons in a semiconductor film to increase the population of excited states, and 4) local heating thermal upon light absorption of the plasmonic structure may enhance the photoelectrochemical reaction rates.[30, 31] Challenges and potential solutions of these experimental studies are described in our recent perspective.[11] One of the challenges is the stability of plasmonic metal during PEC measurements such as photocorrision of plasmonic metal to form metal oxides which will weaken the enhancement capability and cause errors in evaluating their PEC activities.

Herein, we report the wavelength-dependent open-circuit potentials (OCPs) of Au NP-modified $TiO_2$ NRs photoelectrode in a three-electrode system. PEC testing under OCP conditions will retain the stability of plasmonic metal since there is no significant charge to be collected from the surface under light illumination. The transient growth and decay of negative photopotential $E_p$ can be separately analyzed to obtain the photogenerated charge accumulation and relaxation kinetics. Direct experimental observation of the photogenerated charge accumulation can be realized by mapping the growth rate of $|E_p|$, where the plasmonic effect is resolved. The charge relaxation kinetics in the dark is described with a nonexponential kinetics model illustrating the averaged relaxation lifetime and the lifetime

distribution. In addition, different sizes and geometries of Au layer on $TiO_2$ NRs can be studied for elucidating the structural influence on the photogenerated charge transfer. We also construct a single-particle dark-field scattering (DFS) spectroscopy technique with improved action spectra collection efficiency to acquire the plasmon-induced light scattering information of the single Au@$TiO_2$ NRs.

## 2. Experimental

*2.1 Reagents and materials.* Titanium (IV) n-butoxide ($Ti[O(CH_2)_3CH_3]_4$, >99%) from Alfa Aesar, potassium bicarbonate and sodium citrate dihydrate from Fisher Scientific, silver nitrate from EMD Millipore, polyvinylpyrrolidone (PVP, K 30, wt ~40000) from Fluka Analytical, hydrochloric acid (HCl, 37% wt.), acetone (≥ 99.5%), and ethanol (≥ 95%) from VWR were used as received without any further purification. ITO-coated glass (< 15 Ω/sq.) was bought from Colorado Concept Coatings, LLC. FTO-coated glass (TEC15, < 15 Ω/sq.) was purchased from Pilkington. Au (99.999%) for electron beam evaporation was supplied by Kurt J. Lesker Company.

*2.2 Single-particle dark-field scattering spectroscopy.* The preparation of single $TiO_2$ and Au10@$TiO_2$ NRs on ITO was performed as follows. $TiO_2$ and Au10@$TiO_2$ grown on FTO substrates were pretreated with a layer of 1 wt.% PVP in ethanol and dried in air. $TiO_2$ or Au10@$TiO_2$ NRs were then scratched off the FTO surface and dispersed in 1 wt.% PVP in ethanol by bath ultrasonication for 1 h. A cleaned (with the same cleaning procedures of FTO glass) ITO glass slide was spin-coated with the NRs dispersion at 1000 rpm for 10 s and then 2000 rpm for 60 s and dried in air. The as-prepared single NRs coated ITO glass was seated on an inverted microscope (Olympus IX-71) equipped with a 40×/0.75 NA objective lens and an electron-multiplying charge-coupled device (EM-CCD) camera ((iXon X3 DU-897E, Andor Technology). A top light illumination was introduced through an optical fiber from the same light source used in the OCP measurement without applying the UV blocking filter. A dark field condenser (0.86 NA) was used to create incident light from side directions so that the scattered light can be collected by the objective and detected by an EM-CCD camera. Darkfield scattering images were taken at -50 °C with an applied gain of 100 and an exposure time of 0.1 s. The background extraction and particle trajectory tracking were achieved using custom MATLAB programs.

*2.3 Preparation of $TiO_2$ NRs on FTO Glass.* A typical hydrothermal process was used to prepare $TiO_2$ NRs on FTO glass.[32] Specifically, the 2 cm × 2 cm FTO glass slides were used as substrates and cleaned by sonicating for 20 min each in detergent solution, acetone, ethanol, and DI water. The substrates half-covered with Polytetrafluoroethylene (PTFE) tape were sited vertically at the bottom of a 25 mL stainless-steel Teflon-lined autoclave, where the precursor solution containing 0.3 mL titanium(IV) butoxide in 20 mL 18.5% wt. HCl was transferred. The hydrothermal process was performed in an electric oven at 180 °C for 4 h. After being cooled down to room temperature, samples were completely rinsed with DI water and then annealed at 450 °C in the air for 2 h.

*2.4 Au modification of $TiO_2$ NRs on FTO Glass.* Au layers with thicknesses of 1, 5, 10, 50, and 100 nm were deposited at the as-prepared $TiO_2$ nanostructures (denoted as Au1@$TiO_2$, Au5@$TiO_2$, Au10@$TiO_2$, Au50@$TiO_2$, and Au100@$TiO_2$, respectively) with an electron beam evaporation system. Au deposition was conducted at a rate of 1 Å $s^{-1}$ and a vacuum pressure of ~$5 \times 10^{-6}$ Torr. The annealing process of Au@$TiO_2$ samples was performed at 450 °C in the air for 1 h. Surface morphology and Au/Ti atomic ratio were characterized using a field-emission scanning electron microscopy (Apreo FE-SEM, Thermo Scientific) equipped with an energy dispersive X-ray spectrometer (EDX, Bruker X-Flash SD detector).

*2.5 Open-circuit potential measurements.* The front-side light illumination was provided by a Newport 66902 Xenon Arch lamp equipped with an Oriel AM 1.5 solar simulator filter and a monochromator (MD-1000, Optical Building Blocks Corp.). The full lamp intensity without using a monochromator was 100 mW/$cm^2$. A Thorlabs GG400 long-pass UV blocking filter was applied to minimize interferences from the intense absorption of UV light at $TiO_2$. A shutter was used for on-off control of the light illumination. The OCPs were measured by a CHI760 potentiostat (CH Instruments Inc., Austin, TX) in a three-electrode system including the as-prepared $TiO_2$ or Au@$TiO_2$ as working electrode (WE), Ag/AgCl (saturated KCl) as reference electrode (RE), and graphite rod as a counter electrode (CE).

## 3. Results and Discussion

*3.1 Morphological and elemental characterizations of $TiO_2$ and Au-modified $TiO_2$ NRs on FTO glass.*

SEM was used to characterize the surface morphology of $TiO_2$ and Au@$TiO_2$ hybrid nanostructures on FTO glass. As shown in **Figure 2A**, vertically grown $TiO_2$ NRs can be observed on the FTO surface with an estimated diameter of 100 nm. The formation mechanism in the hydrothermal synthesis has been currently considered to start with the dissolution of hydrate precursor containing

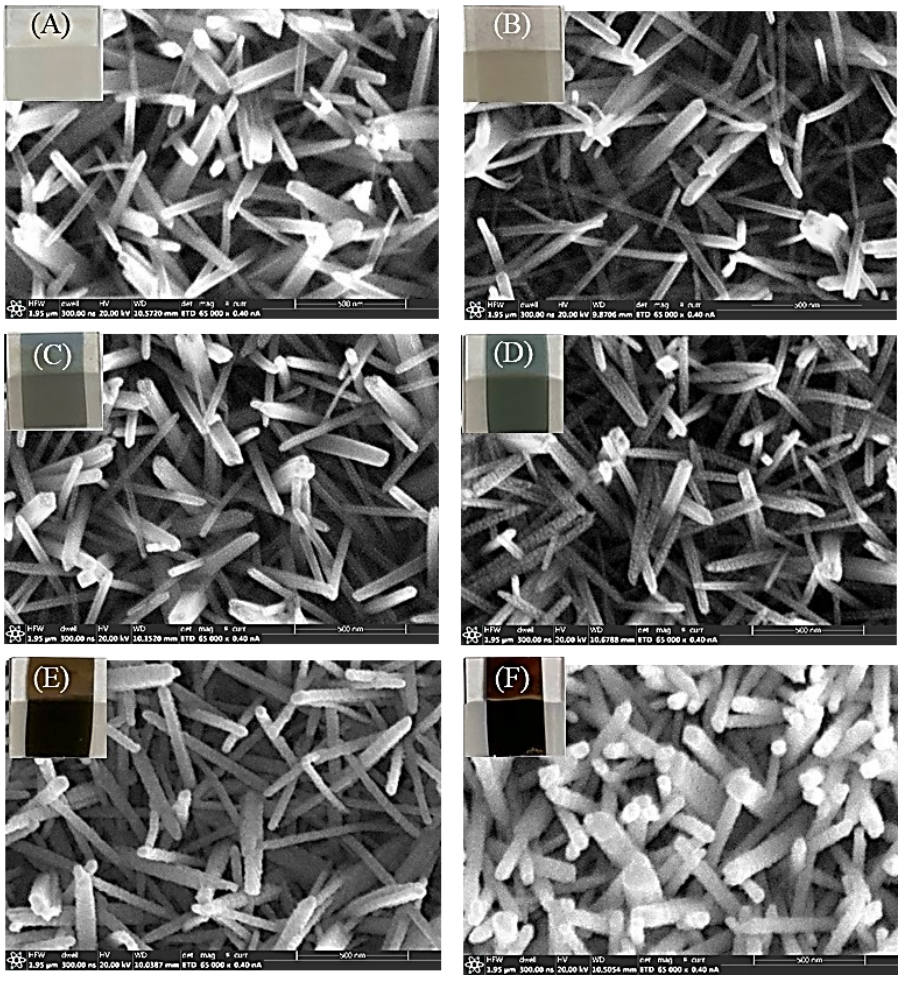


**Fig. 2**. SEM images of the as-prepared (A) bare $TiO_2$/FTO, (B) Au1@$TiO_2$/FTO, (C) Au5@$TiO_2$/FTO, (D) Au10@$TiO_2$/FTO, (E) Au50@$TiO_2$/FTO, and (F) Au100@$TiO_2$/FTO. Insets of SEM images show the corresponding photos of the samples (top half: bare FTO coated with Au; bottom half: $TiO_2$/FTO coated with Au). Scale bars: 500 nm.

titanium ions forming $Ti^{4+}$ hydrated octahedral monomers, $[Ti(OH)_h(H_2O)_{6-h}]^{4-h}$, where hydrolysis ratio (h) was proposed to be critical to determine the connection manner in $TiO_2$ crystal nucleus formed via the following condensation reaction.[33, 34] XRD characterization confirms that $TiO_2$ NRs obtained with the hydrothermal reaction contain both amorphous and crystalline forms of rutile and anatase phases according to our recent report.[32, 35] **Figures 2B-F** are SEM images of $TiO_2$ NRs coated with various thicknesses of Au using electron-beam evaporation. $TiO_2$ NRs show no significant morphological changes upon 5-10 nm Au coating except showing improved surface conductivity as evidenced by the increase in brightness due to enhanced electron scattering. $TiO_2$ NRs coated with Au film show light pink (1 nm Au) and dark blue (5 and 10 nm Au) and dark brownish (50 and 100 nm Au) colors due to strong light absorption and scattering of Au films (inset photos of **Figure 2)**. SEM images of post-annealed Au@$TiO_2$/FTO samples (**Figure S1**) suggested that Au films would form aggregated NPs with growing size and interparticle spacing under thermal annealing conditions as the Au film thickness increases. This is due to the sharply decreased melting point (< 450 °C) of thinner Au film and the fast diffusion of gold clusters to form larger-sized Au structures upon thermal annealing.[36, 37] Some $TiO_2$ NRs are exposed in the annealed Au50@$TiO_2$/FTO and Au100@$TiO_2$/FTO with very large Au NPs (~100-400 nm) embedded in the NRs structure.

EDX was performed to illustrate the thermal annealing effect on the Au/Ti atomic ratios for various thicknesses of Au-TiO2 NR samples. As shown in **Figure S2,** Au/Ti atomic ratio increases significantly for 1 nm and 5 nm Au films upon thermal annealing because of the increase in Au particle sizes resulting in higher visibility in the FE-SEM images than smaller Au NPs. An increase in the sizes of Au NPs upon thermal annealing of 1 and 5 nm films would not help recover $TiO_2$ surface because Au NPs have high surface area coverage on TiO2 NRs. Either a minor or significant decrease in Au/Ti atomic ratio was detected in our very limited data set for 10, 50, and 100 nm Au films, this is because the post-annealing process induces an increase in the Au NP size and the interparticle spacing (**Figure S1**), which significantly results in surface heterogeneities in Au NP and $TiO_2$ NR spatial distribution, yielding in the increase in the visibility of Ti in one area while enhancing the visibility of Au at other areas.

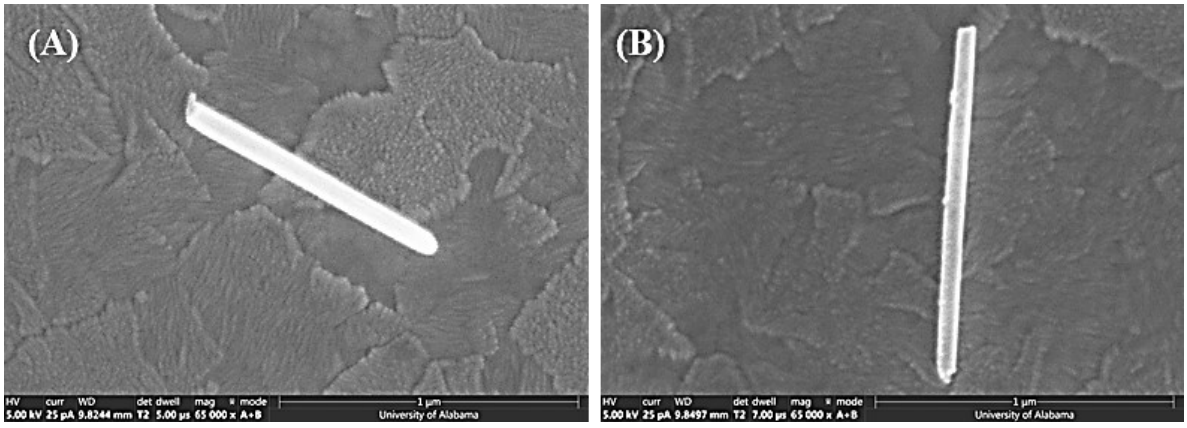


**Fig. 3**. SEM images of a bare $TiO_2$ NR (A) and Au10@$TiO_2$ NR (B) on ITO glass substrate. Scale bars: 1μm.

*3.2 Quantification of light scattering enhancement of Au on $TiO_2$ NRs using single-particle dark-field scattering spectroscopy.* LSPR enhances the optical scattering cross-section in addition to the light absorption.[38] We thus further analyzed the contribution of light scattering of Au NPs in the Au-modified $TiO_2$ NRs system using single-particle DFS spectroscopy. The unannealed Au10@$TiO_2$/FTO was studied as a model system because of sufficient visible light scattering of conformal Au coating and good surface attachment of Au even after thermal annealing, although this single nanoparticle quantification can be used for all other Au@$TiO_2$ samples. The single $TiO_2$ and Au10@$TiO_2$ NRs were scratched from the FTO-supported samples, dispersed with ultrasonication, and then spin-coated on ITO glass. Unfortunately, the aggregations of NRs cannot be thoroughly avoided although a PVP stabilizer was involved. **Figure 3** shows the SEM images of a bare $TiO_2$ NR and Au10@$TiO_2$ NRs on an indium-doped tin oxide (ITO) glass substrate. $TiO_2$ NR surface coated with Au exhibits increased surface roughness due to the small nanoclusters of Au.

**Figure 4A** shows the schematic diagram of a single-particle DFS microscope with monochromator-controlled light illumination. DFS videos of Au10@$TiO_2$ NRs were recorded by the CCD camera while the incident light wavelength is scanned. The merged video images are shown in **Figure 4B**. The individual particle trajectories with background correction were analyzed with custom MATLAB programs and are plotted in **Figure 4C**. Due to the aggregations of NRs, $TiO_2$ and Au10@$TiO_2$ NRs scatter the incident light over the entire visible-light region. However, the characteristic peaks with

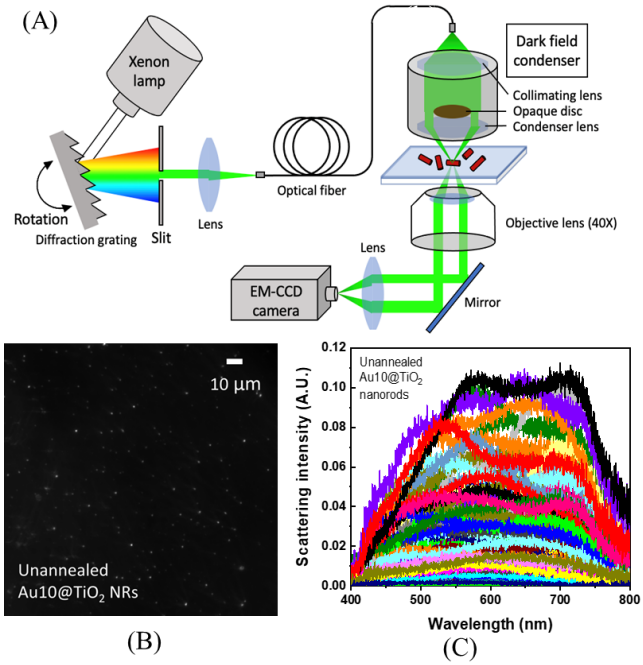


**Fig. 4**. (A) schematic diagram of a single-particle DFS microscope with monochromator-controlled light illumination; Merged DFS video image of unannealed Au10@$TiO_2$ NRs on ITO (B) and corresponding light scattering profiles (C).

stronger light scattering intensities can be helpful to estimate the averaged light scattering properties of these NRs. **Figures 5A and B** present the light scattering intensities at peaks as a function of the corresponding wavelength positions of 340 $TiO_2$ particles and 234 Au10@$TiO_2$ particles. Smaller particles in the DFS images with a less severe aggregation show relatively weak peak intensities, where the statistical wavelength dependency can be obtained. The peak occurrence percentages are calculated by counting the peak occurrence in each wavelength range (**Figure 5C**). Stronger light scatterings occur more frequently within 450-500 and 550-600 nm at both $TiO_2$ and Au10@$TiO_2$. The difference between their peak occurrence percentages reveals the light scattering variation induced by the Au modification (**Figure 5D**). The light scattering is enhanced at 500-600 nm, which corresponds to the plasmonic wavelength range as indicated in the study of photogenerated electron accumulation kinetics at the unannealed Au10@$TiO_2$/FTO using the OCP measurement technique.

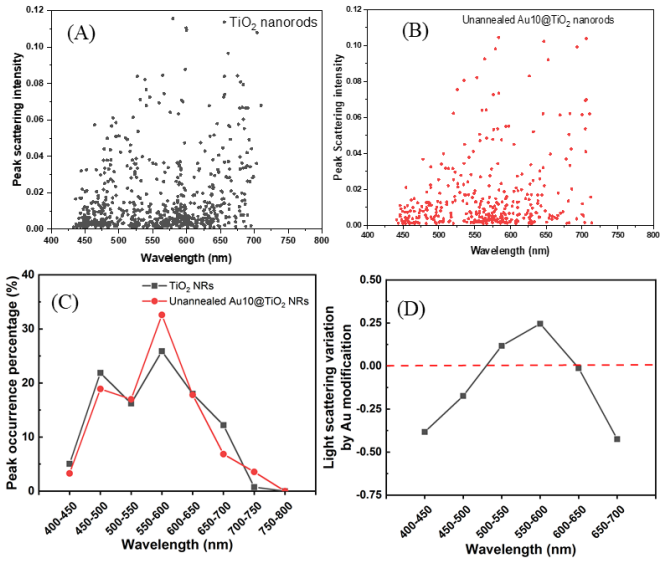


**Fig. 5**. Light scattering intensities at peaks as a function of the corresponding wavelength positions of (A) $TiO_2$ NRs and (B) unannealed Au10@$TiO_2$ NRs. (C) Occurrence percentage of light scattering peaks in different wavelength ranges extracted from (A, B). (D) Light scattering variation by Au modification in different wavelength ranges extracted from (C).

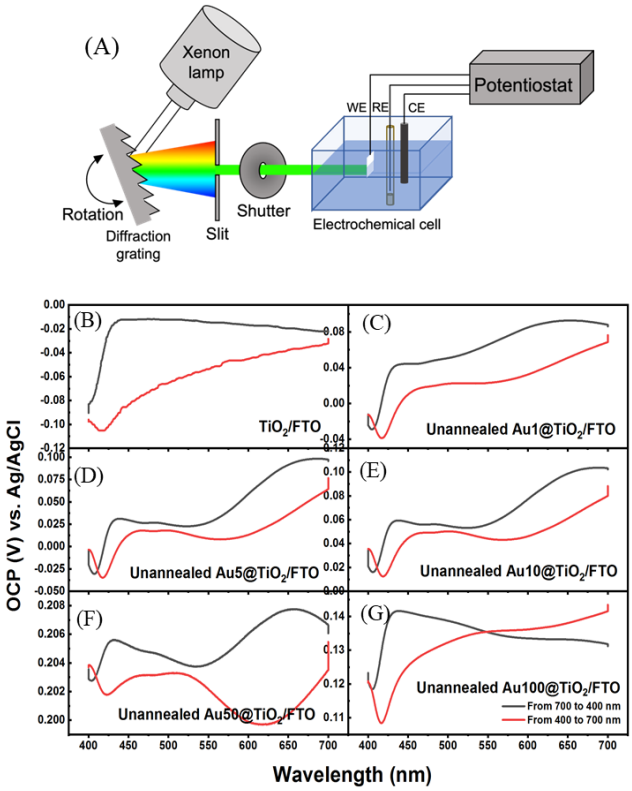


**Fig. 6**. (A) The setup of OCP measurement with tunable incident visible-light wavelength; (B) OCPs of bare $TiO_2$/FTO and (C-G) unannealed Au@$TiO_2$/FTO samples with various Au thicknesses from 1

nm to 100 nm in 0.1 M $KHCO_3$ with excitation wavelengths from 700 to 400 nm (black) and 400 to 700 nm (red) at a wavelength scan rate of 2 nm $s^{-1}$ with a > 400 nm long-pass filter.

*3.3 Quantification of wavelength-dependent charge transfer kinetics of $TiO_2$ and unannealed Au-modified $TiO_2$ NRs by open-circuit potential and photopotential measurements*. The setup of OCP measurement with tunable incident visible-light wavelength is shown in **Figure 6 A**. **Figure 6 B-G** shows the OCP responses of $TiO_2$/FTO, unannealed Au@$TiO_2$/FTO with various Au thicknesses measured under light irradiation with a scanned wavelength at 2 nm $s^{-1}$. When the wavelength is scanned from 700 to 400 nm, OCPs measured in all samples show a negative response below ~438 nm because $TiO_2$ NRs exhibit photoelectrochemical activities of surface defects as revealed in our recent report.[32] Ideally, much more negative potential would be expected when $TiO_2$ NRs are under UV light due to the photoexcitation of electrons to the conduction to increase their quasi-Fermi levels under the open-circuit condition,[39] leading to the negatively shifted electrode potentials, although a > 400 nm UV filter was applied in this study to illustrate visible light activities of Au NPs. Photoexcited electrons may also recombine with the photogenerated holes at some trapping states, for example, the oxygen vacancies and $Ti^{3+}$ defects in $TiO_2$ crystals.[40] When the wavelength is scanned backward from 400 to 700 nm, it shows a delayed recovery of OCPs, owing to the stored charge carriers from the previous cycle. In contrast to the bare $TiO_2$/FTO, Au@$TiO_2$/FTO hybrid structures exhibit negative shifts of OCPs starting from the higher wavelengths in the visible-light region attributed to the plasmonic effect of Au for 5-50 nm Au-coated films, where hot electrons are generated and transferred to the conduction band of $TiO_2$ and then FTO substrate to negatively bias the electrode potential. This peak location is consistent with the peak location measured for a single Au@$TiO_2$ NR shown in **Figure 5**. Such wavelength-dependent plasmonic characteristics for 5-50 nm Au films are not shown in 100 nm Au-coated film (**Figure 6G**) which exhibits strong NIR reflection and scattering instead.

The OCP was thus monitored as a function of incident photon energy by measuring the transient changes during light on and off under single wavelengths. Under the open-circuit condition, the shift of quasi-Fermi level ($E_F^*$) in $TiO_2$ or Au-modified $TiO_2$ upon light illumination from the equilibrium value

($E_{F0}$, which is equal to the fermi level of electrolyte) measured in the dark can be related to the variation in the OCP (i.e., $E_p$) by Equation 1:[41]

$$E_p = \frac{E_F^* - E_{F0}}{q} = \frac{k_B T}{q} \ln\left(\frac{n}{n_0}\right) \qquad (1)$$

where $k_B$ is the Boltzmann constant, $T$ is the temperature, $q$ is the positive elementary charge, and $n$ and $n_0$ are the electron densities under light and in the dark, respectively. The evolution of $E_p$ is thus an indicator of the effective accumulation and relaxation of free charge carriers in the system.

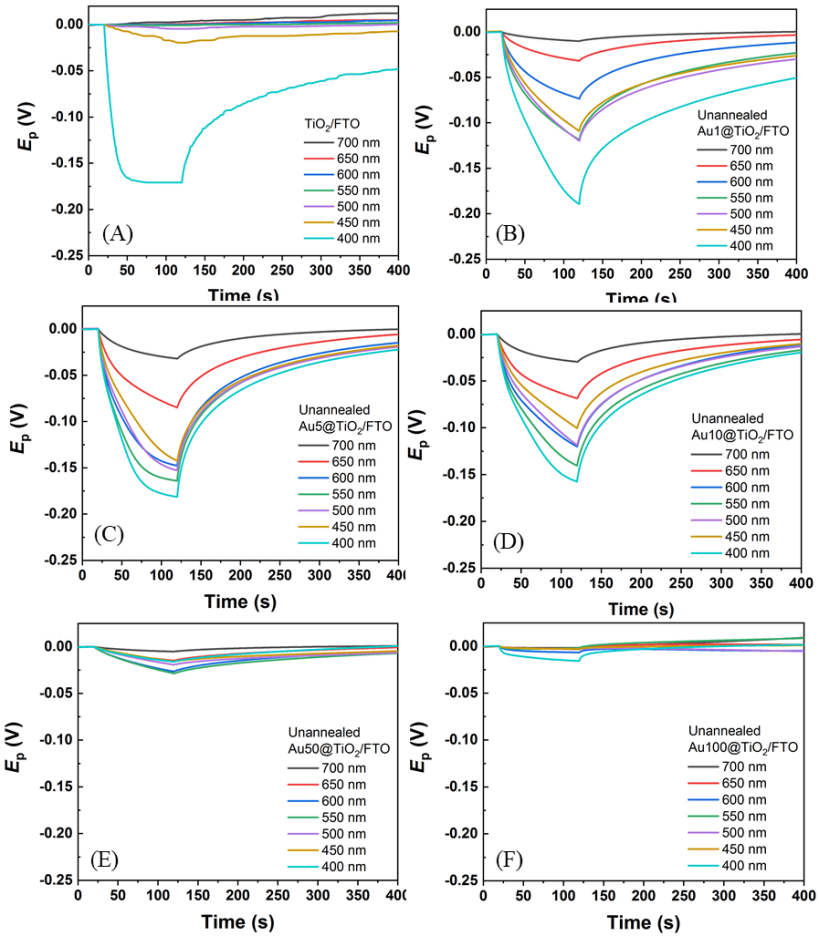


**Fig. 7**. Wavelength-dependent $E_p$ of (A) bare $TiO_2$/FTO and unannealed (B) Au1@$TiO_2$/FTO, (C) Au5@$TiO_2$/FTO, (D) Au10@$TiO_2$/FTO, (E) Au50@$TiO_2$/FTO, and (F) Au100@$TiO_2$/FTO samples 0.1 M $KHCO_3$ with a GG400 long-pass filtered light on at 20 s and off at 120 s.

**Figure 7** presents the transient $E_p$ plots obtained with selected wavelength light on at 20 s and off at 120 s. It can be observed that the $E_p$ rises upon light excitation and tend to reach a plateau at a rate depending on the thickness of Au coating and the incident wavelength. The bare $TiO_2$/FTO develops a

high $E_p$ at 400 nm light illumination, whereas the small Au NPs modified samples (Au1@$TiO_2$/FTO, Au5@$TiO_2$/FTO, and Au10@$TiO_2$/FTO) generate a significant response of $E_p$ under the excitation of visible light. Note that a portion of UV light below 400 nm still leaks through a > 400 nm long-pass filter.

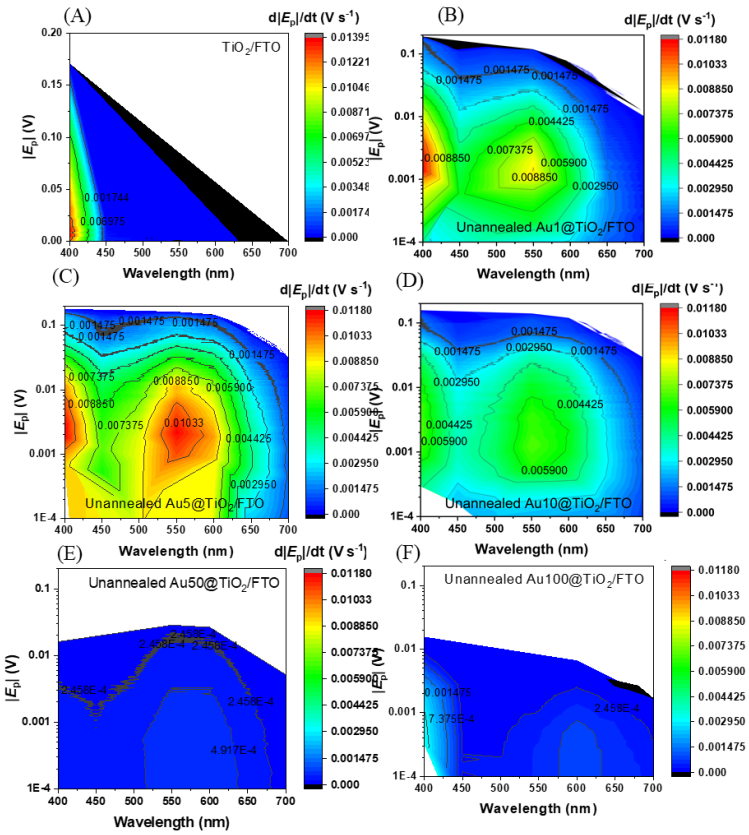


**Fig. 8**. Wavelength-dependent growth rate maps of $|E_p|$ ($d|E_p|/dt$) along with the corresponding $|E_p|$ and incident light wavelength extracted from **Figure 7**. (A) Bare $TiO_2$/FTO; (B) unannealed Au1@$TiO_2$/FTO; (C) unannealed Au5@$TiO_2$/FTO; (D) unannealed Au10@$TiO_2$/FTO; (E) unannealed Au50@$TiO_2$/FTO; (F) unannealed Au100@$TiO_2$/FTO samples.

The accumulation kinetics of the photogenerated electrons at $TiO_2$/FTO and the unannealed Au@$TiO_2$/FTO samples were investigated by mapping the wavelength-dependent growth rate of $|E_p|$ ($d|E_p|/dt$) (**Figure 8**). The bare $TiO_2$/FTO shows a rate of electron generation only upon 400 nm light illumination, but it gradually decreases as the $|E_p|$ reaches a saturation state determined by the incident light intensity. However, the Au@$TiO_2$/FTO samples exhibit a plasmon-enhanced rate of electron accumulation at the visible-light region in addition to 400 nm. These are hot electrons transferred from

the excited states of surface Au. More intense LSPR occurs at small-sized Au NPs (1, 5, and 10 nm), resulting in > 10 times higher electron accumulation rate than the SPR caused by 50 and 100 nm thickness Au coatings. The Au5@$TiO_2$/FTO exhibits the highest rate than Au1@$TiO_2$/FTO and Au10@$TiO_2$/FTO, suggesting a higher charge carrier density, more efficient hot-electron injection upon the appropriate energy level configuration of the Au/$TiO_2$ Schottky barrier, and less charge recombination in the duration of light illumination. It can be observed that the electron accumulation from plasmonic Au is further highly dependent on the incident wavelength. The Au1@$TiO_2$/FTO shows the highest electron accumulation rate at 550 nm which redshifts to 600 nm in the Au100@$TiO_2$/FTO.

This OCP measurement method is thus useful to quantitatively identify the optimal resonant frequency of a plasmonic system. It is particularly superior to conventional optical absorption spectroscopy that cannot be directly applied to some substrate-supported opaque samples. More importantly, mapping of d|$E_p$|/dt along with the corresponding |$E_p$| allows an *in situ* observation of the hot-electron accumulation. Taking the Au5@$TiO_2$/FTO as an example, the electron accumulation rate initially increases when a ~1-10 mV of |$E_p$| is built up reaching a maximum rate of 0.0117 V $s^{-1}$ at the |$E_p$| of 2.16 mV. Then the electrons injected from Au NPs continue to accumulate but at a significantly decreasing rate till the saturation |$E_p$|. The electron accumulation occurs in a similar fashion in Au1@$TiO_2$/FTO and Au10@$TiO_2$/FTO. The initial increase of the electron accumulation rate cannot be resolved in Au50@$TiO_2$/FTO and Au100@$TiO_2$/FTO due to the poor hot-electron transfer efficiency in those systems.

The relaxation kinetics of accumulated electrons can be further investigated from the decay plots of $E_p$ in the dark. In the commonly used OCVD method,[7, 42] the decay of open-circuit voltage ($V$) is assumed to follow a simple pseudo-first-order kinetics model of electron-hole recombination.[41] The recombination lifetime of the minority carrier ($\tau_{rec}$) is expressed by equation below:

$$\tau_{rec} = -\frac{k_B T}{q}\left(\frac{dV}{dt}\right)^{-1} \qquad (2)$$

However, a depletion layer (Schottky barrier) is known to exist in the heterojunction of Au/$TiO_2$, where more complex cooperative charge carrier relaxation pathways are involved. For example, the transfer of hot electrons from the conduction band of $TiO_2$ back to Au may occur when the light is turned off.[43]

Moreover, the trapping and de-trapping of electrons at defects should be taken into account.[41] Bertoluzzi et al. defined an instantaneous relaxation lifetime ($\tau_{ir}$) by Equation 3 for a more general photoactive system:[44]

$$\tau_{ir}(V) = \left(-\frac{1}{V}\frac{dV}{dt}\right)^{-1} \quad (3)$$

For an exponential decay, $\tau_{ir}$ keeps constant. This instantaneous relaxation model is useful to identify the type of non-exponential relaxation dynamics.[44]

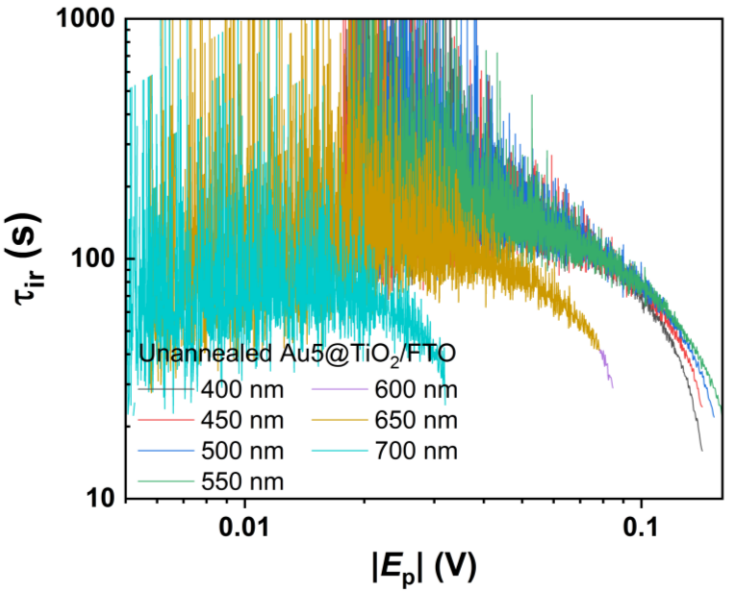


**Fig. 9**. $\tau_{ir}$ as a function of $|E_p|$ for the unannealed Au5@TiO$_2$/FTO extracted from Figure9c.

$\tau_{ir}$ responses of unannealed Au5@TiO$_2$/FTO as a function of $|E_p|$ at various excitation wavelengths are shown in **Figure 9**. It is found to follow the characteristic Kohlrausch-Williams-Watts (KWW) stretched exponential kinetics described by Equations 4 and 5:[44]

$$|E_p| = |E_{p0}| exp\left[-\left(\frac{t}{\tau_{KWW}}\right)^{\beta}\right] \quad (4)$$

$$\langle\tau_{KWW}\rangle = \tau\Gamma[(1/\beta) + 1] \quad (5)$$

where $\Gamma$ denotes the mathematical gamma function, $E_{p0}$ is the initial amplitude of $E_p$, $\tau_{KWW}$ is the characteristic time constant, $\langle\tau_{KWW}\rangle$ is the weighted average relaxation lifetime, and $\beta$ is dimensionless between 0 and 1 and represents the distribution width of the electron lifetime. $\beta = 1$ means a single lifetime. The KWW function is one of the commonly used relaxation models to describe the complex charge transfer kinetics in some dye-sensitized semiconductors and perovskite heterojunctions.[45-47]

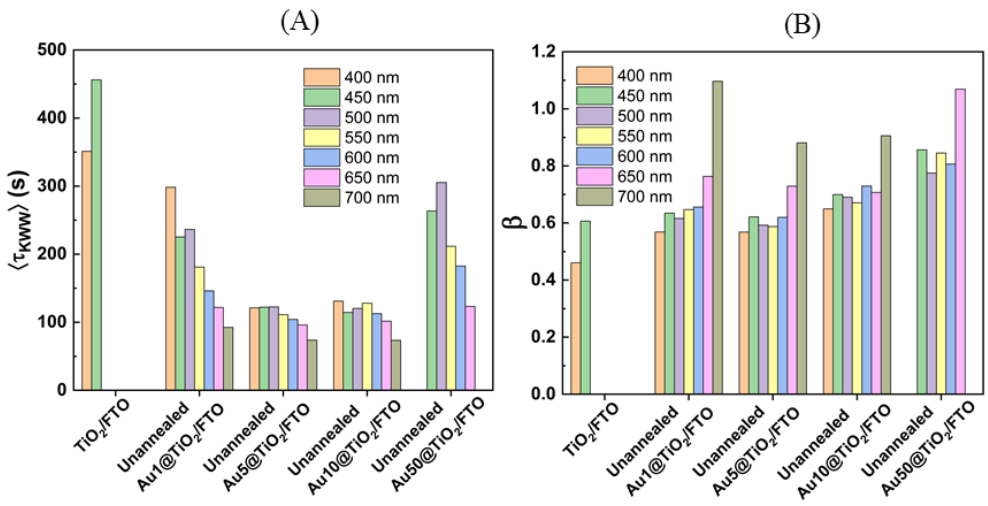


**Fig. 10**. (a) $\langle\tau_{KWW}\rangle$ and (b) $\beta$ obtained by fitting the $|E_p|$ decay curves of $TiO_2$/FTO and unannealed Au@$TiO_2$/FTO samples with the KWW kinetics model ($R^2 > 0.99$).

$\tau_{KWW}$, $\beta$, and $\langle\tau_{KWW}\rangle$ obtained through data fitting of the $|E_p|$ decay curves of $TiO_2$/FTO and unannealed Au@$TiO_2$/FTO samples are summarized in **Table S1**. Wavelength-dependent $\langle\tau_{KWW}\rangle$ and $\beta$ are further plotted in **Figure 10**. The $TiO_2$/FTO exhibits the longest relaxation lifetime (~400 s) after the 400 and 450 nm light excitation, however, it shows low values of $\beta$ suggesting a very broad distribution of lifetime. There could be abundant deep and shallow defects in the NRs array structure of $TiO_2$, like $Ti^{3+}$ and oxygen vacancies, where the accumulated free carriers upon light excitation can be trapped. Deep traps in the energy band prevent the fast charge recombination leading to this long lifetime effect,[48] which is sensitive to the redox species in the electrolyte. In contrast, relatively shorter relaxation lifetimes and higher $\beta$ values are obtained for the Au-modified $TiO_2$ samples after 400 nm light excitation. This is due to the well-dispersed Au NPs (especially in Au5@$TiO_2$/FTO and Au10@$TiO_2$/FTO) that can act as electron reservoirs efficiently preventing the photogenerated electrons from trapping at the deep defects of $TiO_2$.[49] During the plasmonic visible-light excitation, electrons in the conduction band of $TiO_2$ are directly injected from the Au excited state, and fewer charges are trapped in the deep defects of $TiO_2$, so a fast charge relaxation with a short lifetime is expected. It is also known that the photogenerated hot electrons can quickly transfer back to the Au and recombine with the remaining holes if the Schottky barrier between $TiO_2$ and Au is sufficiently low, but this usually occurs within the ps to sub-ns scale and should not account for the >

1 min averaged relaxation lifetime in this case.[50] At longer wavelengths in the visible-light region, limited charge carriers are generated resulting in a fast relaxation and a narrow distribution of lifetime.

*3.4 Effects of post-thermal annealing on the wavelength-dependent charge transfer kinetics of Au-modified $TiO_2$ NRs.* The role of post-thermal annealing in the air on the photogenerated charge carrier transport was further studied in this Au-modified $TiO_2$ NRs system. As shown in **Figure S3**, OCPs of the annealed Au@$TiO_2$/FTO samples illuminated with a scanned wavelength light source suggest that action spectra of OCP curves shift negatively compared to those of the unannealed samples, which is particularly significant for Au1@$TiO_2$/FTO, Au50@$TiO_2$/FTO, and Au100@$TiO_2$/FTO. Thermal treatment in an oxygen-rich environment can effectively reduce the surface oxygen vacancies in $TiO_2$ and decrease the Fermi level of $TiO_2$.[51] The OCP measured between the Fermi levels of $TiO_2$ and the electrolyte is thus decreased. To better observe the build-up and decay of $E_p$, transient OCPs with the light on and off were recorded and the background in the dark was corrected. The $E_p$ values accumulated within the same period become overall more negative after the thermal annealing but with various degrees depending on the incident wavelength and the thickness of the Au layer.

The electron accumulation kinetics under different wavelength excitation (**Figure S4**) can be further analyzed with the growth rate maps of $|E_p|$. The electron accumulation rate under 400 nm illumination generally increases after removing shallow oxygen vacancies in $TiO_2$ during thermal annealing. These shallow defects are primarily fast charge recombination centers hindering the electron accumulation at the $TiO_2$ conduction band. Moreover, an increased surface area of $TiO_2$ NRs is exposed in Au50@$TiO_2$/FTO and Au100@$TiO_2$/FTO, contributing to the enhanced light absorption at $TiO_2$. The variations in the visible-light region are more complex. The decrease of carrier concentration has been reported to lower the Schottky barrier at an Au/(Nb-doped $TiO_2$) interface.[52] The loss of oxygen vacancies in thermal annealing thus leads to a reduced Schottky barrier height (SBH) between the Au NPs and $TiO_2$, facilitating the hot-electron injection when excited with visible light. This becomes the dominant contributing factor in Au5@$TiO_2$/FTO and Au10@$TiO_2$/FTO. However, the size of Au NPs plays another important role in determining the SBH. Ruffino et al. observed the SBH dependency on the Au cluster size in an Au/SiC contact where the SBH dramatically increases with an increased Au cluster size within 5 nm.[53] That the annealed Au1@$TiO_2$/FTO shows a large decrease in the electron

accumulation rate can be explained by the increase of NP size and thus a larger SHB after the thermal annealing. The increase in the electron accumulation kinetics for Au50@$TiO_2$/FTO and Au100@$TiO_2$/FTO can be negligible due to the weak plasmonic effects of the large-sized Au NPs. Another finding after the thermal annealing is that the maximum electron accumulation rates occur at the slightly higher wavelengths due to the increased Au NP sizes, which can be obviously observed in Au5@$TiO_2$/FTO, Au10@$TiO_2$/FTO, and Au50@$TiO_2$/FTO.

The relaxation kinetics of photogenerated charge carriers on the annealed Au@$TiO_2$/FTO samples was investigated by fitting the measured $|E_p|$ decay curves (**Figure S5**) with the KWW function. **Table S1** summarizes $\tau_{KWW}$, $\beta$, and $\langle\tau_{KWW}\rangle$ obtained by KWW function fitting the $|E_p|$ decay curves of annealed Au@$TiO_2$/FTO samples with the KWW kinetic model ($R^2 > 0.99$). Our study suggested that the charge relaxations in the annealed Au1@$TiO_2$/FTO at the plasmonic wavelengths are largely facilitated mainly due to an increased SBH and fewer electrons are injected into the $TiO_2$ conduction band and then trapped at surface defects in $TiO_2$. More hot electrons are recombined with holes left at Au NPs, which is further confirmed by the increased $\beta$. The relaxation lifetimes of Au5@$TiO_2$/FTO and Au10@$TiO_2$/FTO increase with broader distributions after thermal annealing, suggesting that more charges are trapped at different deep sites in $TiO_2$ due to the reduced SBH with more hot-electron injection and charge trapping. The decreased lifetimes and increased $\beta$ values of Au50@$TiO_2$/FTO mainly resulted from its morphology change from Au film to dispersed NPs introducing more fast recombination centers at Au. However, when the annealed Au50@$TiO_2$/FTO generates an enhanced plasmonic effect at 600 nm, more hot electrons are injected into $TiO_2$ with a higher probability to be trapped at the various deep sites. The charge relaxation thus shows a longer lifetime with a broader distribution.

**4. Conclusions**

In summary, we quantitatively investigate the wavelength-dependent charge accumulation and relaxation kinetics at a plasmonic Au-modified $TiO_2$ NRs system by using a simple OCP method for measuring the transient generation and decay of negative $E_p$. The key findings of this study are summarized below:

a. The kinetics analysis of the growth rate of $|E_p|$ of plasmon-induced hot-electron accumulation at the Au-coated $TiO_2$ NRs illustrates a maximum electron accumulation rate of > 10 mV $s^{-1}$ for (Au5@$TiO_2$) in the first a few mVs of $|E_p|$ followed by a decrease at a higher $|E_p|$.

b. The decay of $|E_p|$ of this Au@$TiO_2$ NRs is found to follow a KWW model showing a stretched exponential charge relaxation kinetics. The averaged relaxation lifetime of the Au@$TiO_2$ NRs can be above 1 min and has a broad lifetime distribution, possibly due to the charge trapping at various deep defects, such as oxygen vacancies, which is further confirmed by the study of thermally annealed Au@$TiO_2$ samples.

c. Wavelength dependency of the electron accumulation kinetics is mainly dominated by the LSPR effect of facilitated hot-electron injection in the hybrid nanostructures with different Au sizes and geometries. The relaxation kinetics is further influenced by the wavelength-dependent charge accumulation mechanisms via either the direct hot-electron injection from Au or the photoexcitation of valence band electrons in $TiO_2$.

d. A single-particle DFS spectroscopy platform can be used to investigate the plasmon-induced light scattering variation of the single Au@$TiO_2$ NRs. The wavelength range with strong light scattering can be fast obtained with statistical data analysis of over 200 particles at a time. The enhanced light scattering in the characteristic plasmonic wavelength range of 500-600 nm shows a good agreement with the facilitated electron accumulation kinetics obtained from the OCP study. Although single particle analysis in this report is still preliminary due to the complexity of the Au-coated $TiO_2$ NRs and the interference of strong light scattering of bare $TiO_2$ NRs, further optimization of particle size and surface attachment would allow more accurate analysis of plasmonic effect at single nanoparticle level. This method would potentially allow us to resolve the PEC activities of single NRs by imaging their DFS and wavelength dependence characteristics.

**Declaration of competing interest**

The authors declare that they have no known competing financial interests or personal relationships that could have appeared to influence the work reported in this paper.

**Acknowledgments:** We acknowledge National Science Foundation for supporting this work under Award Number CBET-2113505. S.P. acknowledges the support of Marilyn Williams Elmore and John Durr Elmore Professor fellowship.

## References

[1] L. Wang, M. Hasanzadeh Kafshgari, M. Meunier, Optical Properties and Applications of Plasmonic‐Metal Nanoparticles, Adv. Funct. Mater., 30 (2020) 2005400.
[2] P. Wang, M.E. Nasir, A.V. Krasavin, W. Dickson, Y. Jiang, A.V. Zayats, Plasmonic Metamaterials for Nanochemistry and Sensing, Acc. Chem. Res., 52 (2019) 3018-3028.
[3] B. Du, L. Lin, W. Liu, S. Zu, Y. Yu, Z. Li, Y. Kang, H. Peng, X. Zhu, Z. Fang, Plasmonic Hot Electron Tunneling Photodetection in Vertical Au–Graphene Hybrid Nanostructures, Laser Photonics Rev., 11 (2017) 1600148.
[4] B. Feng, J. Zhu, B. Lu, F. Liu, L. Zhou, Y. Chen, Achieving Infrared Detection by All-Si Plasmonic Hot-Electron Detectors with High Detectivity, ACS Nano, 13 (2019) 8433-8441.
[5] C. Clavero, Plasmon-Induced Hot-Electron Generation at Nanoparticle/Metal-Oxide Interfaces for Photovoltaic and Photocatalytic Devices, Nat. Photonics, 8 (2014) 95-103.
[6] A. Sousa-Castillo, M. Comesaña-Hermo, B. Rodríguez-González, M. Pérez-Lorenzo, Z. Wang, X.-T. Kong, A.O. Govorov, M.A. Correa-Duarte, Boosting Hot Electron-Driven Photocatalysis through Anisotropic Plasmonic Nanoparticles with Hot Spots in Au–$TiO_2$ Nanoarchitectures, J. Phys. Chem. C, 120 (2016) 11690-11699.
[7] J.S. DuChene, B.C. Sweeny, A.C. Johnston‐Peck, D. Su, E.A. Stach, W.D. Wei, Prolonged Hot Electron Dynamics in Plasmonic‐Metal/Semiconductor Heterostructures with Implications for Solar Photocatalysis, Angew. Chem. Int. Ed., 53 (2014) 7887-7891.
[8] Y. Kang, Y. Gong, Z. Hu, Z. Li, Z. Qiu, X. Zhu, P.M. Ajayan, Z. Fang, Plasmonic Hot Electron Enhanced $MoS_2$ Photocatalysis in Hydrogen Evolution, Nanoscale, 7 (2015) 4482-4488.
[9] Y. Zhang, W. Guo, Y. Zhang, W.D. Wei, Plasmonic Photoelectrochemistry: In View of Hot Carriers, Adv. Mater., 33 (2021) 2006654.
[10] L. Guo, H. Yin, M. Xu, Z. Zheng, X. Fang, R. Chong, Y. Zhou, L. Xu, Q. Xu, J. Li, In Situ Generated Plasmonic Silver Nanoparticle-Sensitized Amorphous Titanium Dioxide for Ultrasensitive Photoelectrochemical Sensing of Formaldehyde, ACS Sens., 4 (2019) 2724-2729.
[11] S. Pan, M. Ashaduzzaman, X. Li, E. Wornyo, Understanding the nanoscale interactions of surface plasmon-mediated semiconductor surfaces with water and light for renewable energy harvesting and conversion, Current Opinion in Electrochemistry, 37 (2023) 101174.
[12] Y. He, H. Zhang, Z. Wang, Z. Zheng, P. Wang, Y. Liu, H. Cheng, X. Zhang, Y. Da, B. Huang, Photoelectrochemical Oxidation of Amines to Imines and Production of Hydrogen through Mo-Doped $BiVO_4$ Photoanode, ACS Omega, 7 (2022) 12816-12824.
[13] W. Yang, R.R. Prabhakar, J. Tan, S.D. Tilley, J. Moon, Strategies for Enhancing the Photocurrent, Photovoltage, and Stability of Photoelectrodes for Photoelectrochemical Water Splitting, Chem. Soc. Rev., 48 (2019) 4979-5015.
[14] Y. Yang, S. Niu, D. Han, T. Liu, G. Wang, Y. Li, Progress in Developing Metal Oxide Nanomaterials for Photoelectrochemical Water Splitting, Adv. Energy Mater., 7 (2017) 1700555.

[15] P.S. Archana, N. Pachauri, Z. Shan, S. Pan, A. Gupta, Plasmonic Enhancement of Photoactivity by Gold Nanoparticles Embedded in Hematite Films, J. Phys. Chem. C, 119 (2015) 15506-15516.
[16] J. Wang, S. Pan, M. Chen, D.A. Dixon, Gold Nanorod-Enhanced Light Absorption and Photoelectrochemical Performance of α-Fe2O3 Thin-Film Electrode for Solar Water Splitting, J. Phys. Chem. C, 117 (2013) 22060-22068.
[17] S. Pan, Surface enhanced visible light photocurrent and switching behavior of metal oxide semiconductor electrodes modified with plasmonic nanoparticles, ECS Trans., 77 (2017) 1559-1569.
[18] C. Xu, H. Geng, R. Bennett, D.A. Clayton, S. Pan, Ti@TiO2 Nanowire Electrode with Polydisperse Gold Nanoparticles for Electrogenerated Chemiluminescence and Surface Enhanced Raman Spectroelectrochemistry, J. Phys. Chem. C, 117 (2013) 1849-1856.
[19] Z. Shan, D. Clayton, S. Pan, P.S. Archana, A. Gupta, Visible Light Driven Photoelectrochemical Properties of Ti@TiO2 Nanowire Electrodes Sensitized with Core-Shell Ag@Ag2S Nanoparticles, J. Phys. Chem. B, 118 (2014) 14037-14046.
[20] X. Zhang, Y. Zhu, X. Yang, S. Wang, J. Shen, B. Lin, C. Li, Enhanced visible light photocatalytic activity of interlayer-isolated triplex Ag@SiO2@TiO2 core-shell nanoparticles, Nanoscale, 5 (2013) 3359-3366.
[21] J. Lee, S. Mubeen, X. Ji, G.D. Stucky, M. Moskovits, Plasmonic Photoanodes for Solar Water Splitting with Visible Light, Nano Lett., 12 (2012) 5014-5019.
[22] S. Mubeen, J. Lee, N. Singh, S. Kraemer, G.D. Stucky, M. Moskovits, An autonomous photosynthetic device in which all charge carriers derive from surface plasmons, Nat. Nanotechnol., 8 (2013) 247-251.
[23] H. Zhang, G. Wang, D. Chen, X. Lv, J. Li, Tuning Photoelectrochemical Performances of Ag-TiO2 Nanocomposites via Reduction/Oxidation of Ag, Chem. Mater., 20 (2008) 6543-6549.
[24] J. Zheng, H. Yu, X. Li, S. Zhang, Enhanced photocatalytic activity of TiO2 nano-structured thin film with a silver hierarchical configuration, Appl. Surf. Sci., 254 (2008) 1630-1635.
[25] A. Gorzkowska-Sobas, E. Kusior, M. Radecka, K. Zakrzewska, Visible photocurrent response of TiO2 anode, Surf. Sci., 600 (2006) 3964-3970.
[26] L. Sun, J. Li, C. Wang, S. Li, Y. Lai, H. Chen, C. Lin, Ultrasound aided photochemical synthesis of Ag loaded TiO2 nanotube arrays to enhance photocatalytic activity, J. Hazard. Mater., 171 (2009) 1045-1050.
[27] J. He, P. Yang, H. Sato, Y. Umemura, A. Yamagishi, Effects of Ag-photodeposition on photocurrent of an ITO electrode modified by a hybrid film of TiO2 nanosheets, J. Electroanal. Chem., 566 (2004) 227-233.
[28] G. Zhao, H. Kozuka, T. Yoko, Sol-gel preparation and photoelectrochemical properties of TiO2 films containing Au and Ag metal particles, Thin Solid Films, 277 (1996) 147-154.
[29] V. Subramanian, E.E. Wolf, P.V. Kamat, Catalysis with TiO2/Gold Nanocomposites. Effect of Metal Particle Size on the Fermi Level Equilibration, J. Am. Chem. Soc., 126 (2004) 4943-4950.
[30] Y. Dubi, I.W. Un, Y. Sivan, Thermal effects – an alternative mechanism for plasmon-assisted photocatalysis, Chemical Science, 11 (2020) 5017-5027.
[31] L. Mascaretti, A. Naldoni, Hot electron and thermal effects in plasmonic photocatalysis, Journal of Applied Physics, 128 (2020) 041101.
[32] N. Kaneza, P.S. Shinde, Y. Ma, S. Pan, Photoelectrochemical Study of Carbon-Modified p-Type $Cu_2O$ Nanoneedles and n-Type $TiO_{2-x}$ Nanorods for Z-Scheme Solar Water Splitting in a Tandem Cell Configuration, RSC Adv., 9 (2019) 13576-13585.

[33] J. Zhang, P. Sun, P. Jiang, Z. Guo, W. Liu, Q. Lu, W. Cao, The Formation Mechanism of $TiO_2$ Polymorphs under Hydrothermal Conditions Based on the Structural Evolution of $[Ti(OH)_h(H_2O)_{6-h}]^{4-h}$ Monomers, J. Mater. Chem. C, 7 (2019) 5764-5771.
[34] J. Xie, X. Wang, Y. Zhou, Understanding Formation Mechanism of Titanate Nanowires through Hydrothermal Treatment of Various Ti-Containing Precursors in Basic Solutions, J. Mater. Sci. Technol., 28 (2012) 488-494.
[35] X. Li, S. Pan, Transparent Ultramicroelectrodes for Studying Interfacial Charge-Transfer Kinetics of Photoelectrochemical Water Oxidation at TiO2 Nanorods with Scanning Electrochemical Microscopy, Analytical Chemistry, 93 (2021) 15886-15896.
[36] P. Buffat, J.P. Borel, Size Effect on the Melting Temperature of Gold Particles, Phys. Rev. A, 13 (1976) 2287.
[37] K. Dick, T. Dhanasekaran, Z. Zhang, D. Meisel, Size-Dependent Melting of Silica-Encapsulated Gold Nanoparticles, J. Am. Chem. Soc., 124 (2002) 2312-2317.
[38] E. Hutter, J.H. Fendler, Exploitation of localized surface plasmon resonance, Adv. Mater., 16 (2004) 1685-1706.
[39] P.J. Cameron, L.M. Peter, Characterization of Titanium Dioxide Blocking Layers in Dye-Sensitized Nanocrystalline Solar Cells, J. Phys. Chem. B, 107 (2003) 14394-14400.
[40] M. Kong, Y. Li, X. Chen, T. Tian, P. Fang, F. Zheng, X. Zhao, Tuning the Relative Concentration Ratio of Bulk Defects to Surface Defects in $TiO_2$ Nanocrystals Leads to High Photocatalytic Efficiency, J. Am. Chem. Soc., 133 (2011) 16414-16417.
[41] A. Zaban, M. Greenshtein, J. Bisquert, Determination of the Electron Lifetime in Nanocrystalline Dye Solar Cells by Open‐Circuit Voltage Decay Measurements, ChemPhysChem, 4 (2003) 859-864.
[42] S.F. Hung, F.X. Xiao, Y.Y. Hsu, N.T. Suen, H.B. Yang, H.M. Chen, B. Liu, Iridium Oxide‐Assisted Plasmon‐Induced Hot Carriers: Improvement on Kinetics and Thermodynamics of Hot Carriers, Adv. Energy Mater., 6 (2016) 1501339.
[43] X.-C. Ma, Y. Dai, L. Yu, B.-B. Huang, Energy Transfer in Plasmonic Photocatalytic Composites, Light Sci. Appl., 5 (2016) e16017-e16017.
[44] L. Bertoluzzi, R.S. Sanchez, L. Liu, J.-W. Lee, E. Mas-Marza, H. Han, N.-G. Park, I. Mora-Sero, J. Bisquert, Cooperative Kinetics of Depolarization in $CH_3NH_3PbI_3$ Perovskite Solar Cells, Energy Environ. Sci., 8 (2015) 910-915.
[45] L. D'Amario, L.J. Antila, B. Pettersson Rimgard, G. Boschloo, L. Hammarstrom, Kinetic Evidence of Two Pathways for Charge Recombination in NiO-Based Dye-Sensitized Solar Cells, J. Phys. Chem. Lett., 6 (2015) 779-783.
[46] A. Pockett, G.E. Eperon, N. Sakai, H.J. Snaith, L.M. Peter, P.J. Cameron, Microseconds, Milliseconds and Seconds: Deconvoluting the Dynamic Behaviour of Planar Perovskite Solar Cells, Phys. Chem. Chem. Phys., 19 (2017) 5959-5970.
[47] L. Troian-Gautier, B.N. DiMarco, R.N. Sampaio, S.L. Marquard, G.J. Meyer, Evidence that $\Delta S^{\ddagger}$ Controls Interfacial Electron Transfer Dynamics from Anatase $TiO_2$ to Molecular Acceptors, J. Am. Chem. Soc., 140 (2018) 3019-3029.
[48] B. Choudhury, A. Choudhury, Oxygen Defect Dependent Variation of Band Gap, Urbach Energy and Luminescence Property of Anatase, Anatase–Rutile Mixed Phase and of Rutile Phases of $TiO_2$ Nanoparticles, Phys. E: Low-Dimens. Syst. Nanostructures, 56 (2014) 364-371.
[49] A. Stevanovic, S. Ma, J.T. Yates Jr, Effect of Gold Nanoparticles on Photoexcited Charge Carriers in Powdered $TiO_2$−Long Range Quenching of Photoluminescence, J. Phys. Chem. C, 118 (2014) 21275-21280.
[50] C. Bauer, J.-P. Abid, H.H. Girault, Hot Adsorbate-Induced Retardation of the Internal Thermalization of Nonequilibrium Electrons in Adsorbate-Covered Metal Nanoparticles, J. Phys. Chem. B, 110 (2006) 4519-4523.

[51] T.-T. Nguyen, K.A. Dao, T.T.O. Nguyen, T.D.T. Ung, D.T. Nguyen, S.H. Nguyen, Unexpected Impact of Oxygen Vacancies on Photoelectrochemical Performance of Au@$TiO_2$ Photoanodes, Mater. Sci. Semicond. Process., 127 (2021) 105714.
[52] Y. Jiao, A. Hellman, Y. Fang, S. Gao, M. Käll, Schottky Barrier Formation and Band Bending Revealed by First-Principles Calculations, Sci. Rep., 5 (2015) 1-8.
[53] F. Ruffino, M. Grimaldi, F. Giannazzo, F. Roccaforte, V. Raineri, Size-Dependent Schottky Barrier Height in Self-Assembled Gold Nanoparticles, Appl. Phys. Lett., 89 (2006) 243113.